



# Strong Soft X-Ray Excess in 2015 *XMM-Newton* Observations of BL Lac OJ 287

Main Pal<sup>1</sup> , Pankaj Kushwaha<sup>2,3</sup> , G. C. Dewangan<sup>4</sup> , and P. K. Pawar<sup>4</sup>

<sup>1</sup> Centre for Theoretical Physics, Jamia Millia Islamia, New Delhi 110025, India; [rajanmainpal@gmail.com](mailto:rajanmainpal@gmail.com)

<sup>2</sup> Department of Astronomy (IAG-USP), University of Sao Paulo, Sao Paulo 05508-090, Brazil; [pankaj.tifr@gmail.com](mailto:pankaj.tifr@gmail.com)

<sup>3</sup> Aryabhata Research Institute of Observational Sciences (ARIES), Nainital 263002, India

<sup>4</sup> Inter University Centre for Astronomy and Astrophysics (IUCAA), Pune 411007, India

Received 2019 June 14; revised 2019 December 20; accepted 2019 December 27; published 2020 February 11

## Abstract

We report a strong soft X-ray excess in the BL Lacertae  $\gamma$ -ray blazar OJ 287 during long exposure in 2015 May, among two of the latest *XMM-Newton* observations performed in 2015 and 2018 May. In the case of the 2015 May observation, a log parabola model fits the EPIC-pn data well, while a log parabola plus a power law describes the overall simultaneous optical to X-ray spectra, suggesting the excess as the synchrotron tail. This interpretation, however, is inconsistent with the observed spectral break between near-infrared (NIR) and optical spectra, attributed to a standard disk around a supermassive black hole (SMBH). Based on this, we considered two commonly invoked accretion-disk-based models in active galactic nuclei (AGNs) to explain the soft excess: the cool Comptonization component in the accretion disk and the blurred reflection from the partially ionized accretion disk. We found that both cool Comptonization and blurred reflection models provide an equally good fit to the data, and favor a super-heavy SMBH of mass  $\sim 10^{10} M_{\odot}$ . Further investigation of about a month-long simultaneous X-ray and ultraviolet (UV) pointing observations revealed a delayed UV emission with respect to the 1.5–10 keV band, favoring X-ray reprocessing phenomenon as the dominant mechanism. The results suggest that the soft excess is probably caused by strong light bending close to the SMBH. The detected soft excess in the 2015 data and its disappearance in the 2018 data is also consistent with the presence of accretion-disk emission, inferred from the NIR–optical spectral break between 2013 May and 2016 March.

*Unified Astronomy Thesaurus concepts:* Galaxy nuclei (609); X-ray active galactic nuclei (2035); Active galaxies (17); High energy astrophysics (739); Galaxy jets (601); Relativistic disks (1388); Blazars (164); BL Lacertae objects (158); Supermassive black holes (1663)

## 1. Introduction

OJ 287 ( $z = 0.306$ ) is one of the most luminous and rapidly variable BL Lacertae objects (BLLs) at radio to optical frequencies (Sitko & Junkkarinen 1985; Stickel et al. 1989). It is also one of the most extensively studied extragalactic active galactic nuclei (AGNs) over the entire electromagnetic spectrum from radio waves to  $\gamma$ -rays (Visvanathan & Elliot 1973; Hudec et al. 2013; Valtonen et al. 2016; Gupta et al. 2017; Britzen et al. 2018; Goyal et al. 2018; Kapanadze et al. 2018; Kushwaha et al. 2018a, 2018b and references therein). Apart from the typical stochastic variability of blazars and favorable observational properties like high radio and optical brightness, the most prominent features responsible for making the source famous are the presence of a recurrent regular optical outburst about every 12 years (Sillanpaa et al. 1988, 1996a) and its double-peaked structure (Sillanpaa et al. 1996b).

Two interpretations have been suggested in the literature for the regular optical outbursts. One class of models attributes the quasi-periodic outbursts to the interaction dynamics of accretion disk and supermassive black holes (SMBHs; Sillanpaa et al. 1988; Lehto & Valtonen 1996) in a binary SMBH system, while the other class of models attributes it to the Doppler-boosted jet emission as a consequence of geometrical alignment of precessing single (Britzen et al. 2018 and references therein) or double relativistic jets (Qian 2018 and references therein). The very first model by Sillanpaa et al. (1988) explained the periodicity to increased

accretion flow due to tidal disturbances induced by the secondary SMBH in the accretion disk of primary SMBH. The model was modified after the observation of a sharp rise during the 1994 and 1996 outbursts by Lehto & Valtonen (1996), who attributed the periodicity and double-peaked structure as the impact of secondary SMBH on the primary accretion disk. The disk-impact binary SMBH model has been fairly successful in predicting the timing of the double-peaked  $\sim 12$  yr quasi-periodic outbursts (Hudec et al. 2013; Valtonen et al. 2016). It attributes the flare emission to thermal bremsstrahlung of the hot gas torn off during the impact, and constrains the SMBH masses to  $\sim 1.8 \times 10^{10} M_{\odot}$  and  $\sim 1.5 \times 10^8 M_{\odot}$  for the primary and secondary SMBHs, respectively (Valtonen et al. 2012, 2016). The geometrical class of models, on the other hand, argues a total system mass in the range of a few times  $\sim 10^7$ – $10^9 M_{\odot}$  (Shi et al. 2007; Britzen et al. 2018; Qian 2018 and references therein).

From the shape of the broadband energy spectra, it is known that OJ 287 is a low-peaked BLL with the peak of the low-energy hump, attributed to synchrotron emission from the jet, at near-infrared (NIR) energies. The high-energy hump in the X-ray to  $\gamma$ -ray band normally peaks at  $\sim 100$  MeV (Abdo et al. 2010; Kushwaha et al. 2013). The synchrotron self-Compton (SSC) mechanism successfully describes it as typical X-ray emission, while  $\gamma$ -ray emission is shown to be due to the inverse Comptonization of a  $\sim 250$  K ( $\sim 0.022$  eV) torus photon field (EC-IR Kushwaha et al. 2013), contrary to the generally believed SSC origin of high-energy hump in BLLs. However, during its latest multiwavelength activity from 2015 December to 2017 July, OJ 287 exhibited a hardened MeV–GeV

emission, showing a clear shift in the peak of the high-energy hump to GeV energies (Kushwaha et al. 2018a, 2018b). At the same time, a spectral break between NIR–optical emission was also observed for the first time as reported by Kushwaha et al. (2018a). The occurrence of NIR–optical spectral break was traced back to 2013 May (MJD 57439) and continued since then until 2016 March. They further showed that the observed MeV–GeV spectral change can be naturally reproduced by external Comptonization, but this time by inverse Compton (IC) of broadline region photons (Kushwaha et al. 2018a), which have been detected during the previous cycles of  $\sim 12$  yr optical outbursts (Nilsson et al. 2010). The NIR–optical spectral break is most naturally explained by the standard disk emission of a  $\sim 10^{10} M_{\odot}$  SMBH. Interestingly, its first appearance in 2013 May (MJD 56439; Kushwaha et al. 2018a, 2019) is very close to the impact time predicted in the disk-impact binary SMBH model (Lehto & Valtonen 1996) in the BH frame. This spectral and temporal coincidence currently tilts the central engine debate in the favor of disk-impact binary SMBH model.

A survey of the literature records show that OJ 287 has exhibited the most dramatic spectral variations in X-ray energy band. The reported spectral shapes cover all of the possible energy-spectral profiles, from a power law—the typical X-ray spectrum of OJ 287 (Seta et al. 2009; Abdo et al. 2010; Kushwaha et al. 2013)—to flat ones (e.g., Siejkowski & Wiercholska 2017; Kushwaha et al. 2018b) and extremely soft spectra (e.g., Isobe et al. 2001; Kushwaha et al. 2018b), as well as a mixture of these (e.g., Isobe et al. 2001; Valtonen et al. 2012; Kushwaha et al. 2018a). As already mentioned, the typical power-law X-ray energy spectra are successfully described by SSC emission (Seta et al. 2009; Kushwaha et al. 2013), while the flat and mix spectra (typical+soft) have been argued to be as a result of a mixture of synchrotron and the SSC emission (Isobe et al. 2001; Siejkowski & Wiercholska 2017) in one interpretation. The other possibility that has been proposed but not yet studied, is an additional spectral component like Bethe–Heitler emission. The extremely soft X-ray spectra observed during the 2016–2017 activity is shown to be a new, additional high-frequency-peaked BLL (HBL) emission component (Kushwaha et al. 2018b), thanks to the coordinated multiwavelength followups. In light of this, the extremely soft X-ray spectra (Isobe et al. 2001) that were observed earlier as well could be the HBL component. Interestingly, within the limit of available records, strongly soft X-ray spectra seem to be a common feature of the source, present within a few years around the  $\sim 12$  yr quasi-periodic optical outbursts.

In this work, we perform spectral study of the 2015 and 2018 *XMM-Newton* observations of OJ 287, supplementing it with multiple *Swift* X-Ray Telescope (XRT)/UltraViolet and Optical Telescope (UVOT) observations to explore the soft X-ray excess in the 2015 *XMM-Newton* data. In Section 2, we present details of observation and data reduction. Section 3 presents the systematic spectral analysis of data and results. In Section 4, we report our discussion. A summary and conclusions are presented in Section 5. We used the cosmological parameters  $H_0 = 67.04 \text{ km s}^{-1} \text{ Mpc}^{-1}$ ,  $\Omega_m = 0.3183$  and  $\Omega_{\Lambda} = 0.6817$ <sup>6</sup> to calculate the distance.

## 2. Observation and Data Reduction

OJ 287 has been observed multiple times by *XMM-Newton* observatory, mainly around the  $\sim 12$  yr quasi-periodic optical outbursts. Some of the previous observations have been studied in detail (Gupta et al. 2016; Gaur et al. 2018). The latest observation with  $\sim 28$  ks and the longest exposure ( $\sim 129$  ks) of this object were performed in 2018 April (MJD = 58149–58150) and 2015 May (MJD = 57149–57150), respectively. The European Photon Imaging Camera (EPIC)-pn (Turner et al. 2001) was operated in the prime large window mode with the thin filter during both the observations. We also used *Swift* XRT/UVOT observations from MJD = 57140.4 to MJD = 57173.6. This period includes the 2015 May *XMM-Newton* observation.

We followed the standard reduction procedure using the *XMM-Newton* Science Analysis System (SAS v15.0) (Gabriel et al. 2004) with latest calibration files. First, we reprocessed the EPIC-pn data using `epproc` and obtained event files. We removed the intervals affected by flaring particle background by examining light curves above 10 keV to get events file. We used single and double events (PATTERN  $\leq 4$ ) for the EPIC-pn, and omitted events at the CCD edges and bad pixels (FLAG = 0). We extracted the source spectrum using a circular region of  $50''$ , centered at the source. We also obtained a background spectrum from a circular region of the same size away from the source and free from any sources. The resulted net exposures were found to be  $\sim 53$  ks and  $\sim 19$  ks for the 2015 and 2018 observations, respectively. The net count rates in 2–10 keV band were observed to be  $0.316 \pm 0.003$  and  $0.299 \pm 0.004 \text{ counts s}^{-1}$  for the 2015 and 2018 data sets, respectively. We also examined the pileup very carefully using `epatplot`. We did not find any significant pileup that might affect our analysis. Finally, we generated response matrix and ancillary response files at the source position using the tools `rmfgen` and `arfgen`, respectively. We grouped the data using the SAS task `specgroup` with an oversampling of 3, and minimum counts of 20 per bin.

For the reduction of *Swift* XRT and UVOT data, we followed the steps described in Pal & Naik (2018). We selected background annular region from  $10''$  to  $20''$  centered at the source coordinates. We also omitted the data points from bad patches of the CCD in case of UVOT observations.

## 3. Data Analysis

### 3.1. Spectral Analysis

#### 3.1.1. X-Ray Emission

We used XSPEC v12.10.1 (Arnaud 1996) to analyze the X-ray spectra of OJ 287 and used the  $\chi^2$  statistics for the model fitting. Unless stated otherwise, the errors on the best-fit parameters are quoted at 90% confidence level, corresponding to  $\Delta\chi^2 = 2.706$ .

We considered only EPIC-pn data due to its high signal-to-noise ratio compared with the EPIC-MOS. We began by fitting the 2–10 keV band with an absorbed power law (`tbabs × powerlaw`) model. We fixed the absorption column to the Galactic value of  $N_H = 3.04 \times 10^{20} \text{ cm}^{-2}$  (Dickey & Lockman 1990). This resulted in a  $\chi^2/\nu$  of 157.8/116 and 93.2/97 for the 2015 and 2018 April data, respectively, where  $\nu$  stands for the degree of freedom. The best-fit power-law photon index  $\Gamma$  was found to be  $1.91 \pm 0.03$  and  $2.06 \pm 0.06$

<sup>6</sup> <http://www.kempner.net/cosmic.php>

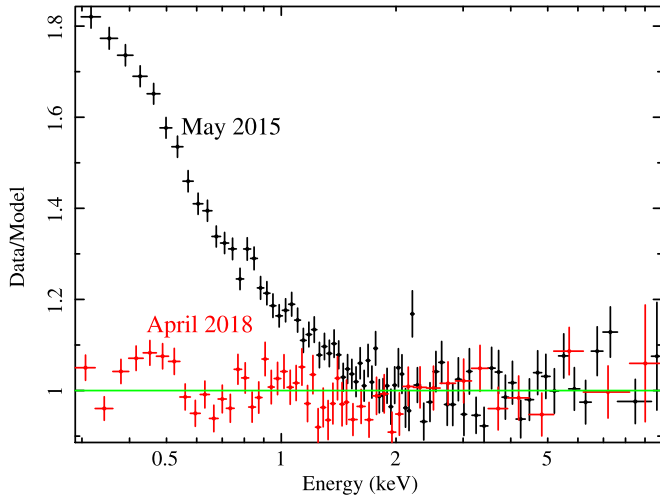


**Figure 1.** Ratio (Data/Model) plot of absorbed power-law model fitted in 2–10 keV band and then extended to 0.3–2 keV. A clear soft excess is present at low energies in the 2015 May data, while the 2018 data seems consistent with a power-law model.

for the two data sets. Thus, both data sets represent a different spectral state of the source. We then extrapolated the best-fit model down to 0.3 keV for both the observations, as shown in Figure 1. Surprisingly, the 2015 May data revealed a strong soft X-ray excess, observed rarely in BLLs, but commonly observed in radio-quiet AGNs, such as the narrowline Seyfert type 1 (NLS1; Leighly 1999; Gierliński & Done 2004; Crummy et al. 2006). To investigate this, we then systematically fitted the whole range (0.3–10 keV) with possible phenomenological models, starting first with log parabola (logpar) and broken power-law emission (bknpower), and then additionally using thermal bremsstrahlung (bremss) as per claims in the literature (Valtonen et al. 2016), and finally the two AGNs models: cool Comptonization (Done et al. 2012; optxagn) and blurred reflection (Miniutti & Fabian 2004; Dauser et al. 2013, i.e., relxill).

A simple powerlaw model fit to the 2015 data over 0.3–10 keV band resulted in a poor fit ( $\chi^2/\nu = 893.7/160$ ) due to the presence of the strong soft excess. As this AGN is a blazar, the X-ray emission may be described phenomenologically by logpar and bknpower, independently. Fitting  $\text{tbabs} \times \text{logpar}$  over 0.3–10 keV band resulted in  $\chi^2/\nu = 202.8/159$  while  $\text{tbabs} \times \text{bknpower}$  fit resulted in  $\chi^2/\nu = 234.6/158$ . The best-fit parameters for both models are listed in Table 1 and the corresponding data, model, and residuals (in  $\sigma$ ) are shown in Figures 2(a) and (b). The logpar fit describes the data fairly well, however, it is not consistent with the broadband emission of the source (see Section 4 and Figure 5).

Another claim is thermal bremsstrahlung radiation (Valtonen et al. 2016) from a  $3 \times 10^5$  K gas (Valtonen et al. 2012) around the expected  $\sim 12$  yr quasi-periodic optical outbursts. This temperature corresponds to  $\sim 25$  eV, and is irrelevant for the observed soft X-ray excess. Nonetheless, we additionally explored a redshifted zbremss model along with the above-considered models. This model has three parameters: plasma temperature, normalization, and the source redshift. We allowed plasma temperature and its normalization to vary. The fit resulted in  $\chi^2/\nu = 211.8/159$ . The best-fitting parameters are listed in Table 1, while the plots are shown in top and bottom panels of Figure 2(c). During model fitting, we

**Table 1**  
Best-fitting Parameters of Models Used to Fit the 0.3–10 keV Band for Two *XMM-Newton* Observations

Model component	2015 May	2018 April
$N_{\text{H(Galaxy)}} (10^{20} \text{ cm}^{-2})$	3.04 (f)	3.04 (f)
<b>Logpar</b>		
Slope ( $\alpha$ )	$2.26 \pm 0.01$	$2.09 \pm 0.01$
Curv. term ( $\beta$ )	$-0.33 \pm 0.02$	$-0.06 \pm 0.04$
Norm.(LP) ( $10^{-3}$ )	$1.07 \pm 0.01$	$1.04 \pm 0.01$
Stat. ( $\chi^2/\nu$ )	202.8/159	168.9/138
<b>Bknpower</b>		
Photon index ( $\Gamma_1$ )	$2.38 \pm 0.03$	$2.11 \pm 0.02$
Photon index ( $\Gamma_2$ )	$1.96 \pm 0.03$	$2.02 \pm 0.05$
$E_{\text{break}}$ (keV)	$1.3 \pm 0.1$	$1.67^{+0.8}_{-0.4} \pm 0.03$
Norm.(BPL)( $10^{-3}$ )	$1.06 \pm 0.02$	$1.04 \pm 0.01$
Stat. ( $\chi^2/\nu$ )	234.6/158	167.3/137
<b>PL+bremss</b>		
Photon index $\Gamma$	$1.96 \pm 0.02$	$2.03^{+0.04}_{-0.05}$
Norm. (nth) ( $10^{-3}$ )	$0.96 \pm 0.02$	$1.00^{+0.04}_{-0.06}$
Plasma temp. ( $\frac{kT_{\text{brem}}}{\text{keV}}$ )	$0.31 \pm 0.02$	$0.42^{+0.21}_{-0.28}$
Norm. (brem) ( $10^{-3}$ )	$4.6^{+0.5}_{-0.4}$	$0.61^{+0.15}_{-0.38}$
Stat. ( $\chi^2/\nu$ )	211.8/159	168.9/137
$f_E$ (0.3–2 keV)	3.1	2.8
$f_E$ (2–10 keV)	2.64	2.5
<b>Nth.+Relxill</b>		
Photon index ( $\Gamma$ )	$2.21^{+0.06}_{-0.12}$	$2.03^{+0.04}_{-0.02}$
Norm.(nth) ( $10^{-3}$ )	$0.86^{+0.07}_{-0.05}$	$0.89^{+0.12}_{-0.11}$
Index1 ( $q_{\text{in}}$ )	$7.1^{+0.30}_{-2.2}$	3 (f)
Index2 ( $q_{\text{out}}$ )	$4.2^{+0.1}_{-0.9}$	3 (f)
Photon index ( $\Gamma$ )	$2.21^{+0.06}_{-0.12}$ (t)	$2.03^{+0.04}_{-0.02}$ (t)
$\log\left(\frac{\text{Ionization par.}}{\text{erg cm s}^{-1}}\right)$	$2.3^{+0.4}_{-0.5}$	$3.3^{+0.3}_{-2.2}$
Inner radius ( $r_g$ )	$1.6^{+0.3}_{-0.1}$	$11.7^{+7.0}_{-9.6}$
Break radius ( $r_g$ )	$4.30^{+1.6}_{-0.01}$	$11.7^{+7.0}_{-9.6}$ (t)
Spin ( $a$ )	$0.99^{+0.01}_{-0.07}$	$0.998^{+0.038}_{-0.954}$
Norm.(refl) ( $10^{-5}$ )	$2.6^{+0.5}_{-1.6}$	$0.14 \pm 0.01$
Stat. ( $\chi^2/\nu$ )	184.7/154	162.3/135
$f_E$ (0.3–2 keV)	3.1	2.8
$f_E$ (2–10 keV)	2.66	2.5
<b>optxagnf</b>		
Acc. rate ( $\frac{L}{L_{\text{edd}}}$ )	$0.044^{+0.016}_{-0.003}$	$0.0084^{+0.0038}_{-0.0011}$
Spin ( $a$ )	$0.996^{+0.002}_{-0.095}$	$0.99^{+0.008}_{-0.25}$
Coronal radius ( $r_g$ )	$6.1^{+6.3}_{-1.3}$	$6.9^{+3.2}_{-0.3}$
Plasma temp. ( $\frac{kT_e}{\text{keV}}$ )	$0.46^{+0.17}_{-0.05}$	$0.37^{+0.86}_{-0.18}$
Optical depth ( $\tau$ )	$9.0^{+0.2}_{-1.6}$	$12.1^{+1.2}_{-9.0}$
Frac. power ( $f_{\text{pl}}$ )	$0.11^{+0.01}_{-0.05}$	$0.67^{+0.29}_{-0.03}$
Photon index ( $\Gamma$ )	$1.88^{+0.05}_{-0.04}$	$2.01^{+0.07}_{-0.03}$
Stat. ( $\chi^2/\nu$ )	188.9/155	168.1/134
$f_E$ (0.3–2 keV)	3.1	2.8
$f_E$ (2–10 keV)	2.66	2.5

**Note.** The flux  $f_E$  is measured in units of  $10^{-12} \text{ ergs s}^{-1} \text{ cm}^{-2}$ . “t” stands for parameter tied to other parameter.

found an statistically acceptable fit with a 25 keV plasma temperature. However, this temperature is too high, dominating the high-energy end of the X-ray and is contrary to the general behavior of blazars.



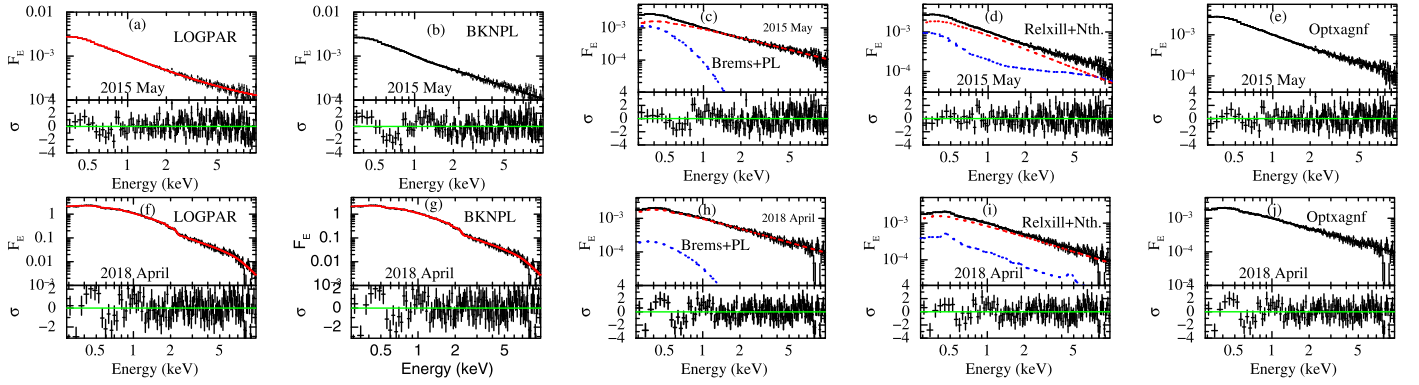


**Figure 2.** Best-fit model data in top panel and residuals (in  $\sigma$ ) in bottom panel are shown for 2015 May (first row) and 2018 April (second row) for models `tbabs*(logpar)` (a, f), `tbabs*(bknpl)` (b, g), `tbabs*(bremss+powerlaw)` (c, h), `tbabs*(relxill+nthcomp)` (d, i), and `tbabs*(optxagnf)` (e, j), respectively (see Section 3). The solid line on the data points represents the net composite model, while dashed lines are different model components of the net composite model. For all of the models, residuals are within 2–3 $\sigma$ .

As an accretion-disk emission has been claimed for the NIR–optical spectral break in a systematic analysis by Kushwaha et al. (2018b), we invoked disk-based soft excess models used to explain the soft X-ray excess normally seen in Seyfert type 1 AGNs (Gierliński & Done 2004; Crummy et al. 2006; Done et al. 2012). Though the origin is still unclear, two competing models—blurred reflection and cool Comptonization—have been the most acceptable. Thus, to a simple absorbed powerlaw model, we added a reflection model `relxill` which is a combination of `xillver` (García et al. 2011, 2013) and `relline` (Dauser et al. 2010, 2013). This model calculates the reflected emission at each angle at each radius of the accretion disk (García et al. 2014). The details of parameters of `relxill` and its different application forms are described briefly on the web page document.<sup>7</sup>

The applied form of `relxill` assumes that the X-ray source illuminates the accretion disk in a lampost geometry (Miniutti & Fabian 2004). The illumination is described as a broken emissivity law that has the form  $\epsilon \propto r^{-q_{\text{in}}}$  between  $r_{\text{in}}$  and  $r_{\text{br}}$ ;  $\epsilon \propto r^{-q_{\text{out}}}$  between  $r_{\text{br}}$  and  $r_{\text{out}}$ ; where  $r$  is the radius of the accretion disk;  $q_{\text{in}}$  and  $q_{\text{out}}$  are inner and outer emissivity indices;  $r_{\text{in}}$ ,  $r_{\text{br}}$ , and  $r_{\text{out}}$  are the inner break and outer radii of the accretion disk. The other parameters are spin ( $a$ ); inclination angle ( $i$ ); iron abundance  $A_{\text{Fe}}$  relative to solar abundance, illuminating power-law index ( $\Gamma$ ); high-energy cutoff ( $E_{\text{cut}}$ ); ionization parameter ( $\xi = L/nr^2$  with  $L$  being the source X-ray luminosity and  $n$  is the hydrogen number density of the disk material); and reflected fraction denoted by  $R$ . We fixed the iron abundance to 1, the inclination to  $3^\circ$ , high-energy cutoff to 300 keV and outer radius to  $400r_g$ . We tied the `relxill` photon index  $\Gamma$  to power-law photon index  $\Gamma$ , hence the  $R$  parameter was fixed to  $-1$  under the lampost scenario. We allowed the rest of the parameters and the fit them with `tbabs*(relxill+powerlaw)` model resulted in  $\chi^2/\nu = 184.6/154$ . To be more realistic, we replaced the phenomenological power-law model by `nthcomp` (Zdziarski et al. 1996; Życki et al. 1999), which can correctly predict the low-energy rollover where Galactic absorption can modify the spectrum. We fixed the seed photon temperature at 2 eV and the electron temperature associated with X-ray corona to 100 keV. The fit resulted in  $\chi^2/\nu = 184.8/154$  with results listed in Table 1, and corresponding plots in the top and bottom panels of Figure 2(d), respectively.

The other widely argued scenario of AGNs soft X-ray excess attributes it to a different plasma embedded in the interior region of the accretion disk. As argued by Done et al. (2012), the gravitational potential energy is released at each point of the accretion disk as a blackbody emission down to  $R_{\text{corona}}$ . Below this radius, the gravitational potential energy is no longer completely thermalized. The energy is distributed into two types of plasma: an optically thick ( $\tau > 1$ ) cool plasma ( $kT_e \sim 0.2$  keV) for soft X-ray excess emission, and an optically thin ( $\tau < 1$ ) hot plasma ( $kT_e \sim 100$  keV) emitting power-law continuum above 2 keV. Thus, to the powerlaw, we added `optxagnf` model, which incorporates the above-mentioned scenario. The important parameters of the model are an accretion rate relative to the Eddington rate  $L/L_{\text{Edd}}$ ; the mass of the BH  $M_{\text{BH}}$  and its spin  $a$ ; the source luminosity distance  $D_L$ ; the cool plasma temperature  $kT_e \sim 0.2$  keV; the optical depth  $\tau$  of cool plasma; the photon index of power-law continuum  $\Gamma$ ; the power fraction of power-law continuum  $f_{\text{pl}}$  and  $R_{\text{corona}}$ . We fixed the  $M_{\text{BH}}$  at  $2 \times 10^{10} M_\odot$  (Valtonen et al. 2016; Kushwaha et al. 2018a),  $D_L$  at 1677 Mpc,  $f_{\text{pl}} = 0$  as the power-law component accounts for the hot Comptonizing component and we fixed the normalization to unity to get proper flux and luminosity for the source. We tied the power-law photon index to the photon index of the `optxagnf` model. The rest of the parameters were allowed to vary. The fit resulted in  $\chi^2/\nu = 189.5/156$ . Furthermore, because `optxagnf` can describe hard X-ray power-law continuum, we varied the parameter  $f_{\text{pl}}$  after removing analytical powerlaw model. This resulted in  $\chi^2/\nu = 189.2/156$  with best-fit model parameters listed in Table 1 and the plot in the top and bottom panels of Figure 2(e), respectively. Additionally, as per other the claims of geometrical models, we also tested  $M_{\text{BH}}$  of  $\sim 10^8 M_\odot$ . However, it resulted in a super Eddington accretion rate of about 1.3 in Eddington units, contrary to the expectation for BLLs.

Application of these models to the 2018 April 0.3–10 keV data did not improve the fit statistics with respect to a simple powerlaw, as can be seen from results in Table 1, and neither it shows any strong soft X-ray excess (see Figure 1).

### 3.1.2. X-Ray to UV/Optical Emission

Statistically, log-parabolic emission (`logpar`), blurred reflection (`relxill`), and cool Comptonization (`optxagnf`) models describe the soft X-ray excess equally well. To

<sup>7</sup> <http://www.sternwarte.uni-erlangen.de/~dauser/research/relxill/>

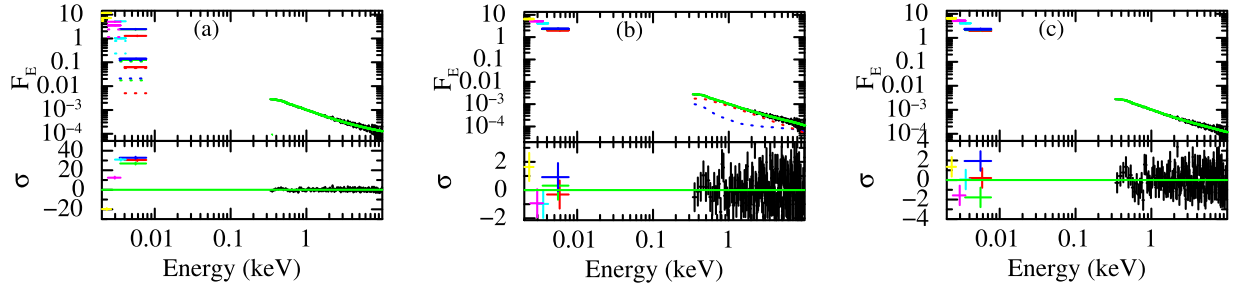


**Figure 3.** Best-fit model data and residuals for (a) `logpar+bremss`. The fit shows strong positive residuals in UV/optical bands (b) `relxill+nthcomp`. (c) `optxagnf`. No significant residuals (within  $2-3\sigma$ ) are present in the UV/optical bands in the best-fitting models related to reflection (b) and Comptonization (c). The solid line on the data points represents the net composite model used here, and the dashed lines are different model components of the net composite model.

distinguish between these models, we used the UVOT data from *Swift* UVOT (MJD = 57149–57150) snapshots, observed simultaneously with the 2015 *XMM-Newton* observation. The extrapolation of best-fitting log-parabolic model of X-rays showed strong residuals in UV/optical band. Having corrected from reddening due to our Galaxy and intrinsic to the source, we added the `zbremss` model to describe the thermal emission as claimed in studies. We found that the `zbremss` with `logpar` results in the worst statistic (see Figure 3(a)). We then extrapolated the best-fit blurred reflection model to UVOT bands and found positive residuals in the low-energy bands. Because the reflection model does not include disk component required for optical/UV spectral break, we added the `diskbb` model with the best-fitting parameters of blurred reflection model. We applied reddening correction due to our Galaxy and intrinsic to the source. We fitted the UV/optical and X-ray bands jointly, which resulted in  $\chi^2/\nu = 189.4/157$ . Similarly, we also fitted the UV/optical/X-ray bands using the disk Comptonization model `optxagnf`, which includes the intrinsic disk emission. Having applied reddening correction, we modeled the full band, and the fit resulted in  $\chi^2/\nu = 201.3/160$ . The best-fit model, data, and residuals are shown in Figures 3(b) and (c) with parameters in Table 2.

### 3.2. Timing Analysis

We examined the timing behavior of OJ 287 2015 May observation to look for lags between X-ray and UV emission. We first checked *XMM-Newton* UVW1 band vis a vis X-rays and did not find any lag between them, suggesting that UV may not be related to X-ray within  $\sim$  day-long observation. In fact, only the optical data of the 2018 observation show a hint of marginal variability, while rest is statistically consistent with no variability. We then used *Swift* -XRT and simultaneous UV observations taken in UVW1 band obtained on a cadence of about half a day during MJD = 57140.4 to MJD = 57187.0, as shown in the upper two panels of Figure 4 (a). Observed light curves are highly variable, and the UV band seems to lag behind the 1.5–10 keV X-rays around MJD = 57170 and afterward. This could be due to reprocessing, as on short timescales OJ 287 normally show simultaneous variability (Kushwaha et al. 2018a, 2013), but has shown lag when an additional competing emission component is present (Kushwaha et al. 2018b). In such cases, the available light curves to date cannot be used for the analysis, due to jet-dominated emission.

We used the *JAVELIN* code (Zu et al. 2011) to estimate the lag following the procedures described in Pal & Naik (2018) and Pal et al. (2017). We found time-lag of  $\sim 3$  and  $\sim 16$  day

**Table 2**  
Best-fitting Parameters of Models Used to Fit the 0.3–10 keV and the UV/Optical Bands Jointly for 2015 Observations

Model component	Model 1	Model 2	
Reddening	$0.13 \pm 0.03$	Reddening	$0.16^{+0.03}_{-0.04}$
Photon index ( $\Gamma$ )	$2.22 \pm 0.08$	Photon index ( $\Gamma$ )	$1.87^{+0.06}_{-0.03}$
$kT_{bb}(nth)$ eV	$2.03^{+0.09}_{-0.03}$	...	...
Norm.(nth) ( $10^{-3}$ )	$0.86^{+0.05}_{-0.03}$	Acc. rate ( $\frac{L}{L_{\text{edd}}}$ )	$0.040^{+0.003}_{-0.004}$
Index1 ( $q_1$ )	$7.2^{+1.7}_{-1.3}$	Coronal radius ( $r_g$ )	$5.7^{+1.9}_{-0.9}$
Index2 ( $q_2$ )	$4.4^{+1.7}_{-1.1}$	Plasma temp. ( $\frac{kT_e}{\text{keV}}$ )	$0.47^{+0.03}_{-0.12}$
Photon index ( $\Gamma$ )	$2.22 \pm 0.08$ (t)	Optical depth ( $\tau$ )	$9.0^{+2.0}_{-0.3}$
$\log(\frac{\text{ionization par.}}{\text{erg cm s}^{-1}})$	$2.3^{+0.1}_{-0.4}$	Frac. power ( $f_{\text{pl}}$ )	$0.12^{+0.05}_{-0.02}$
Inner radius ( $r_g$ )	$1.6 \pm 0.3$	...	...
Spin ( $a$ )	$0.99^{+0.01}_{-0.04}$	Spin ( $a$ )	$0.996^{+0.002}_{-0.006}$
Break radius ( $r_g$ )	$4.2^{+1.7}_{-1.9}$	...	...
Norm.(refl) ( $10^{-5}$ )	$2.7^{+1.1}_{-1.3}$	...	...
$kT_{\text{in}}(\text{disk})$ eV	$2.03^{+0.09}_{-0.03}$ (t)	...	...
Norm.(disk) ( $10^{11}$ )	$3.20 \pm 0.01$	...	...
Stat. ( $\chi^2/\nu$ )	194/156	Stat. ( $\chi^2/\nu$ )	200.9/160

**Note.** Model 1 : Nth.+Relxill+diskbb; Model 2 : Optxagnf. “t” stands for tied parameter in the fit.

for UVW1 compared with X-rays (see Figure 4 (b)). We cross-checked the lag results with the  $z$ -transformed discrete correlation function ( $z\text{DCF}$ ; Alexander 2013), applying the bootstrap technique (Peterson et al. 1998). In the bootstrap method, we extracted 10,000 realizations of the two light curves from the observed light curve pair through Monte Carlo approach by randomizing fluxes and randomly selecting a subset after excluding 20% data points. We then performed cross-correlation on the extracted pairs using the  $z\text{DCF}$  method, as was done between the originally observed light curves. This approach is a model-independent way of accounting for the effects of flux uncertainties and irregular sampling on the cross-correlation result. The lag results from this are shown in Figure 4 (b) and as can be seen clearly, the time-lag range agrees with the one found by the *JAVELIN*.

Within the limitations of data reported here, both the  $\sim 3$  and  $\sim 16$  day lag values are supported by the light curves, shown by plotting a shifted UV light curve with respect to the X-ray in the bottom panels of Figure 4 (a). Further cross-checking with simple discrete cross-correlation ( $\text{DCF}$ ; Edelson & Krolik 1988), we noticed some discrepancies. The three-day lag feature was missing when the full light curves were used (top two panels of Figure 4 (a)), but was recovered when the linear

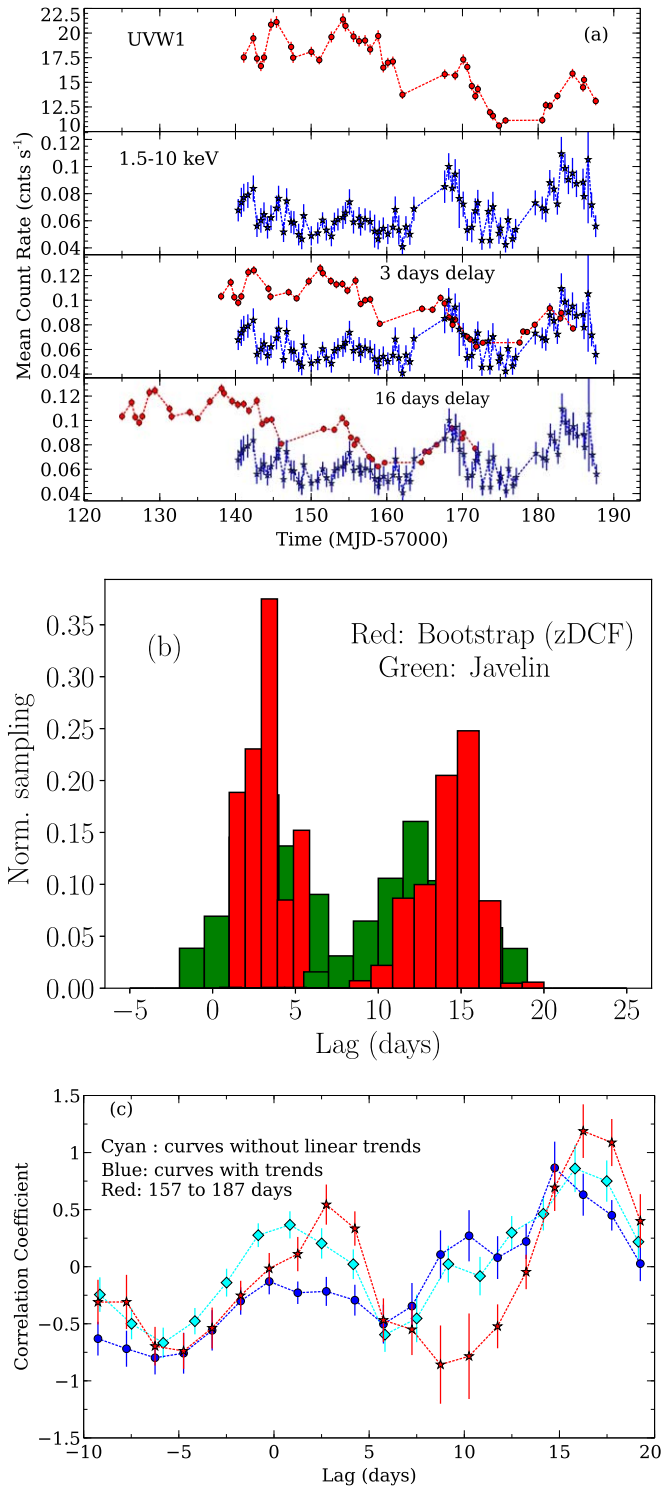


**Figure 4.** (a) Two upper panels show the light curves for UVW1 and 1.5–10 keV bands, while the two lower panels show the UVW1 light curve shifted by  $\sim 3$  and 16 day with respect to the X-ray. Here, the UVW1 count rates are divided by a factor of 170 to match the level with X-ray count rates. (b) Probability distribution of time delay for UVW1 band with respect to the 1.5–10 keV from *Javelin* (green) and *zDCF* (red) codes (see Section 3.2). (c) Lag results from simple DCF method considering different time ranges (red and blue) and by removing the linear trends from the full light curves (the top two panels of 4 (a)).

trends were removed from the light curves, e.g., McHardy et al. (2014, 2018). The three-day lag, however, remains if we consider data after MJD 57157 without even removing the

linear trend from the light curves. These outcomes are shown in Figure 4(c).

In short, while both the lag values are supported by the data, the  $\sim 16$  day lag is consistently present in all the methods while the  $\sim 3$ -day lag is recovered after eliminating the linear trend while performing DCF analysis. Unfortunately, gaps before and after the light curves used, as well as the sampling of available data, do not allow any further analysis (e.g., significance estimate). Regardless, however, there is a clear indication of lag.

#### 4. Discussion

We performed a spectral and temporal study of OJ 287 based on the 2015 and 2018 long *XMM-Newton* observations. Except for a marginal hint of variability in the 2018 *XMM-Newton* optical data, rest is statistically consistent with no variability within each observation ( $\sqrt{\text{variance of rate}} \lesssim \text{mean error in the rate}$ ). Spectrally, however, the two observations represent a very different X-ray spectral state of the source. The 2018 X-ray spectrum shows the most generic spectral state of the source characterized by a power-law spectrum (Isobe et al. 2001; Seta et al. 2009; Kushwaha et al. 2013; Siejkowski & Wiercholska 2017) while the 2015 X-ray spectrum shows strong soft X-ray excess with respect to a power-law spectrum below 2.0 keV (Figure 1, Section 3.1). To best of our knowledge, such (soft X-ray) excesses—the focus of our study here, has been reported only once in OJ 287 (Isobe et al. 2001). We systematically investigated the emission mechanisms behind the origin of this excess using models motivated from blazar and normal AGN studies.

##### 4.1. Blazar-based Models

Blazars are known for variability in all the domains of observation. Spectral changes, as reported in this work, at the low-energy end of the X-ray emission, can physically have multiple origins. In addition to the possibility of an altogether new emission component (e.g., Kushwaha et al. 2018a, 2018b), in the general scheme of blazar emission scenario, an appropriate overlap of synchrotron and SSC component can mimic a variety of phenomenological spectral shapes. The literature records on OJ 287 show only one instance of a similar spectral state in the 1994 ASCA observation. A spectral study by Idesawa et al. (1997) reported a power-law photon spectral index of  $\Gamma \sim 1.67$ . However, a careful reanalysis by Isobe et al. (2001) found that a broken power-law spectrum with a break at 2 keV describe the data statistically better. Furthermore, the spectral index below 2 keV was consistent with the optical/UV spectrum, hence they attributed the soft excess to the “synchrotron soft tail.”

In the current case, we followed a flexible approach and systematically investigated by modeling with both the possible phenomenological spectral shapes: log parabola and broken power-law models. This allows to capture additional contributions (e.g., Isobe et al. 2001; Kushwaha et al. 2018b). Of the two, we found that a log parabola model provides a statistically acceptable description of the 2015 EPIC-pn data (see Table 1). A log parabola spectrum within blazar emission scenarios can simply arise from an appropriate combination of the high-energy end of a simple power-law synchrotron spectrum or its steeply declining part with the rising part of the SSC emission (see Figure 5, bottom panel). A look at the NIR and optical



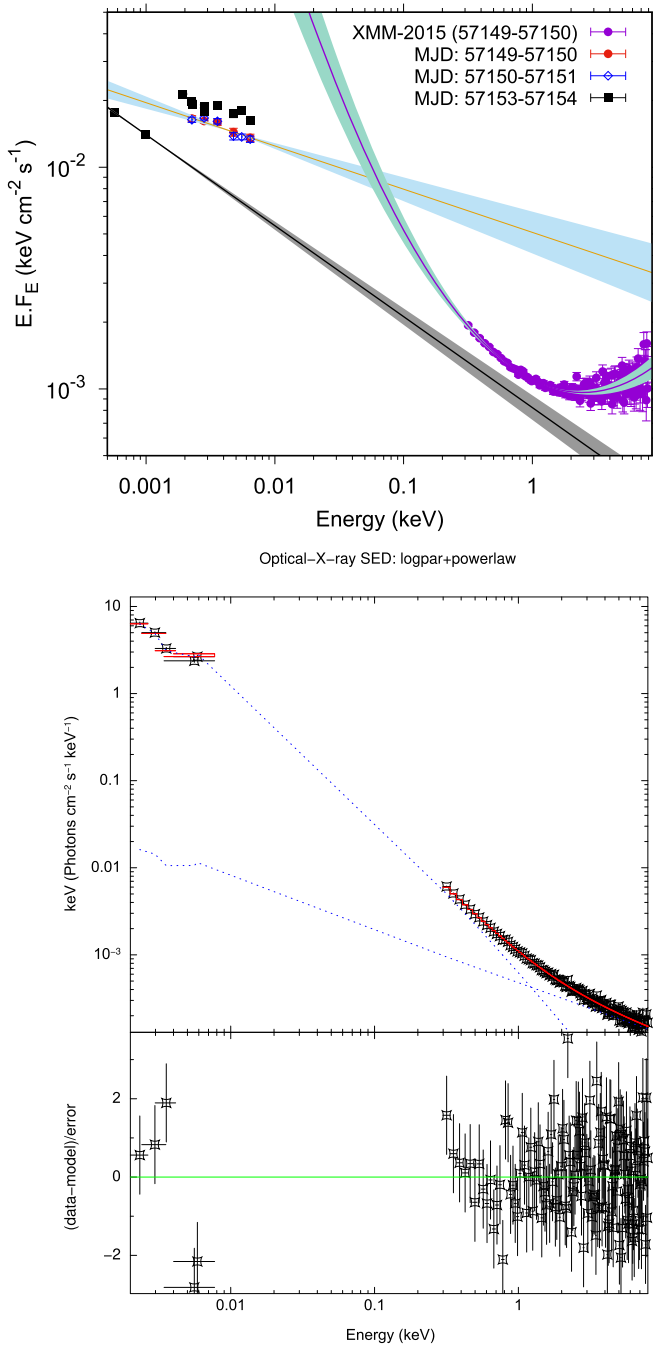


**Figure 5.** Top: NIR to X-ray SEDs of OJ 287 around 2015 *XMM-Newton* observation. The solid curves within the shaded regions are the best-fit log parabola and power-law model to the X-ray and NIR/optical/UV data, respectively, while shaded area represent their  $1\sigma$  range bounded by error in spectral indices only. Bottom: best-fitted log parabola+power-law model to the optical to X-ray emission. The dotted curves are the individual model components (optical to soft-X-ray: log parabola), while the red curve is the sum of the two components.

SEDs around the 2015 observation, as shown in the top plot of Figure 5, clearly show that the soft X-ray excess lies above the simple power-law extrapolation of the NIR data, but below the optical/UV data points. Noting that in the most generic spectral state of OJ 287 the optical-UV data simply lies on a power-law (log parabola) extension of NIR data, the SEDs around 2015 observations suggest two possibilities in the present context. *CASE A*: a synchrotron spectrum associated with NIR data

points extending to X-rays with a power law or steeply declining tail (Figure 5, gray band). *CASE B*: optical/UV being synchrotron with a smoothly declining tail causing the soft X-ray excess (Figure 5, bottom plot). Below, we systematically look into these two possibilities.

*CASE A.* In this case, the optical-UV data remains unexplained, suggesting additional broadband emission component. Attributing the NIR–optical break to accretion-disk emission as suggested in Kushwaha et al. (2018a), the combined emission still failed to reproduce the UV emission (see Figure 6 in Kushwaha et al. 2018a; see also Kushwaha et al. 2019). Thus, though this interpretation could provide a viable explanation for soft X-ray excess, the UV data remain unexplained.

*CASE B.* As shown in Figure 5 (bottom plot), this scenario successfully reproduces the optical/UV to soft X-ray emission by using log parabola model (logpar) when combined with a power law representing the X-ray emission above the soft X-ray band. The combined log parabola plus power law provide an acceptable fit to the data ( $\chi^2/\nu \simeq 1.2$ ). Furthermore, the resulting power-law index of  $\sim 1.6$  for X-ray emission is also consistent with the general X-ray spectra of the source. However, this fails to explain the two NIR data points unless the synchrotron peak of its broadband SED, which normally peaks at NIR (KJ bands; e.g., Seta et al. 2009; Kushwaha et al. 2013) has shifted to optical energies, making NIR data to be part of spectrum before the peak of synchrotron emission. However, an NIR–optical SED comparison with 2009 SED does not support such a shift (Figure 2, Kushwaha et al. 2019). Furthermore, even smoothing of the low-energy end to match one of the NIR data on the basis that low-energy hump peaks around NIR bands (e.g., Isobe et al. 2001; Kushwaha et al. 2013, 2018a) leaves the other NIR data points unexplained. It should be further noted that this is not a one odd observational data, as the NIR–optical SED trend has been like this since 2013 May (MJD 54639) as reported by Kushwaha et al. (2018a). Thus, though phenomenologically logpar description is fine for X-rays, it is not consistent with the broadband emission characteristics of the source during this period, thereby suggesting some other emission components for the soft X-ray excess.

Another proposal in the literature is a dominant thermal bremsstrahlung emission for the  $\sim 12$  yr quasi-periodic optical outbursts from a thermal gas of temperature  $\sim 3 \times 10^5$  K (Valtonen et al. 2016, 2012). However, this temperature corresponds to  $\sim 25$  eV, which is too small to produce the observed excess in 0.1–2 keV (Figure 3(a)). Considering this scenario and keeping the temperature free during the fit, we found an statistically acceptable fit with 25 keV plasma. However, this is unphysical as it dominates the high-energy end of the X-ray emission, and is contradictory to previous studies and the general X-ray spectral profile of the source being a power law. Combination of log parabola (for synchrotron and its high-energy tail), thermal bremsstrahlung, and power law (for SSC) to optical to X-ray data resulted in a very low plasma temperature ( $\sim 0.1$  eV), making the bremsstrahlung ineffective with resulting scenario similar to a power law plus log parabola which, as argued above, are in tension with NIR–optical spectral break.

#### 4.2. Radio-quiet AGN/Disk-based Models

The claim of NIR–optical break as accretion-disk emission of a  $\sim 10^{10} M_{\odot}$  SMBH and its presence between 2013 May (MJD 56439) until 2016 May suggests a disk-based soft X-ray excess origin as in radio-quiet AGNs as potential candidates. We, therefore investigated this possibility with two of the AGN disk dominant models: cool Comptonization (*optxagn*) and blurred reflection, argued for the soft X-ray excess often observed in Seyfert galaxies, e.g., Mrk 509 (Mehdipour et al. 2011), 1H 0707–495 (Fabian et al. 2009), II Zw 177 (Pal et al. 2016), and ESO 113–G010 (Cackett et al. 2013). We found that both cool Comptonization and blurred reflection plus disk describes the data well (like the log parabola model) and are equally acceptable statistically (see Table 1 and Section 3).

In the cool Comptonization scenario, the best fit suggests the observed soft excess is due to inverse Compton scattering of seed photons flux from the disk ( $f_{\text{PL}} \sim 0.1$ , see Table 1) in the cool Comptonizing plasma ( $kT_e \sim 0.4$  keV and  $\tau \sim 10$  in this work). The derived accretion rate for observed soft X-ray excess was found to be  $\sim 10\%$  of Eddington unit. Such a high accretion rate for prominent soft X-ray excess has been seen in a number of radio-loud, narrowline Seyfert type 1 (RLNLS1) AGNs, i.e., 1H 0323+342 (Ghosh et al. 2018). The temperature and optical depth of the cool plasma embedded in the inner region of the accretion disk are inferred to be  $kT_e \sim 0.5$  keV and  $\tau \sim 10$ , respectively, for the soft X-ray excess in 2015 May observation. Such a type of cool plasma has been found in RLNLS1 galaxies i.e., PMN J0948+0022 (D’Ammando et al. 2014). The flux observed for soft excess in the 0.3–2 keV band was found to be  $\sim 3 \times 10^{-12}$  erg s $^{-1}$  cm $^{-2}$ , which is comparable with what is claimed in a RLNLS1 PMN J0948+0022. Thus, the BL Lac object OJ 287 behaves like a radio-loud, narrowline Seyfert galaxies in this particular observation.

Additionally, because SMBH mass is one of the parameter in the cool Comptonization scenario, we also checked it by fitting first a SMBH mass of  $\sim 2 \times 10^{10} M_{\odot}$ , as suggested by NIR–optical break and also in the disk-impact binary SMBH model. This resulted in a accreting rate of  $\sim 0.04$  in Eddington units. Fit with an SMBH mass of  $\sim 1 \times 10^8 M_{\odot}$  as argued by jet-precession based models, on the other hand, resulted in a super Eddington accretion rate  $\sim 1.3$ , contrary to the expectation for BL Lac objects. Thus, the model too supports a very massive SMBH mass as claimed in the binary SMBH and also from the NIR–optical spectral break. It should, however, be noted that central engine mass is not a true discriminator for the two classes of models suggested for  $\sim 12$  yr QPO, as in the geometrical class of models, the central engine mass is not connected directly with the model parameters and is inferred based on other observations, unlike the case of disk-impact binary SMBH model.

In case of X-ray reflection under the lamppost geometry, the blurred reflection is very intense and strong (see Table 1) close to the inner edge of the accretion disk. The emissivity pattern is not uniform, and it changes from inner radius to a break radius  $R_{\text{br}} \sim 4r_g$  (inner emissivity index  $\sim 7$  and outer emissivity index  $\sim 4$ ). Thus, the strong soft excess is likely due to the strong light bending in the vicinity of the central SMBH. The best-known proxy for the blurred reflection is the broad iron- $K\alpha$  emission line near 6 keV (Tanaka et al. 1995). However, the Fe- $K\alpha$  emission line is absent in the 2015 observation, and in fact never been detected in OJ 287 or any BLL to best of our

knowledge. This fit suggests an intense smearing for blurred reflection, too strong for Fe- $K\alpha$  emission line to be seen in the data (see the blue dashed line for blurred reflection in Figure 3(b)). In this scenario, a likely possibility is that the disk may be illuminated by the base of the jet (McHardy et al. 2014, 2018; Pal et al. 2018). We found clear indications of lagging of UVW1 band emission with respect to the hard X-ray emission ( $\sim 3$  and  $\sim 16$  days; see Figure 4). Such lags favor the X-ray reprocessing scenario at the accretion disk, and have been reported in many AGNs where UV is found to be lagging behind X-ray emission as expected in the reprocessing scenario (e.g., McHardy et al. 2014, 2018; Buisson et al. 2017; Pal & Naik 2018). Additional support for this comes from the general variability trend of OJ 287 where multiwavelength variations are normally simultaneous on short timescales (Kushwaha et al. 2018a, 2013) with lag reported only when an additional emission component was competing with its general emission (Kushwaha et al. 2018b).

The best-fit reflection+disk model in the optical/UV/X-ray bands suggests a inner disk temperature of  $\sim 2$  eV (ref. Table 2). We used theoretical temperature profile ( $T(r) \sim 6.3 \times 10^5 \left(\frac{\dot{M}_E}{\dot{M}_8}\right)^{0.25} \left(\frac{r}{R_s}\right)^{-0.75}$ , where  $\dot{M}_E$ ,  $\dot{M}_8$ ,  $R_s$ , and  $r$  are accretion rate in Eddington units, black hole mass in  $10^8 M_{\odot}$ , Schwarzschild radius, and disk radius from the center, respectively) with the best-fit parameter to infer the temperature at the inner edge of the disk. This provided in a temperature of about  $\sim 2.8$  eV, similar to the one inferred from the X-ray/UV/optical modeling, further supporting the disk-impact binary SMBH scenario. Furthermore, the normalization of multicolor blackbody model i.e., *diskbb*, is a function of inner radius of the accretion disk and the luminosity distance along with the inclination of the source. Using inner radius  $R_{\text{in}} = 1.6 r_g$ , mass of the black hole  $M_{\text{BH}} = 2 \times 10^{10} M_{\odot}$ , inclination  $i = 3^\circ$  and luminosity distance 1652.08 Mpc, we derived the normalization value to be  $8.2 \times 10^{10}$ . This is similar with the best-fit value listed in Table 2. Thus, both the observed inner disk temperature and the normalization are in agreement in support for the binary black hole system with a super-heavy super-massive black hole at the center.

Both the AGN disk-based models suggest a maximally rotating SMBH, contrary to the tightly constrained spin value of  $\sim 0.30$  claimed by Valtonen et al. (2016). We tested blurred reflection by fixing the spin parameter at 0.30 and the fit statistic was marginally disfavored ( $\chi^2_{\nu} \sim 1.5$ ). This marginal change for a large change in the value of spin suggests that current data are not sufficient to constrain the spin and/or a detailed comparative study is required based on the theoretical premise of the model.

## 5. Summary and Conclusion

We performed spectral analysis of the two yet unstudied *XMM-Newton* observations of OJ 287 performed in 2015 and 2018, respectively. Temporally, both the data are statistically consistent with nonvariable, but are spectrally very different. We found that while the 2018 data represents the typical (most generic) X-ray spectral state of the source characterized by a power-law spectrum, the 2015 data show very strong soft X-ray excess. The excess lies above the simple power-law extrapolation of the NIR data points but below the best-fit power-law extrapolation of the optical/UV data points. We systematically explored the physical process behind the spectral shape vis a



vis consistency with known/established observational properties of OJ 287 as listed below.

1. For the X-ray spectrum only, a simple log parabola model describes the 2015 spectral state statistically well and can be generated with an appropriate overlap of synchrotron tail extended to X-ray energies and the SSC spectrum. However, this interpretation is in conflict with the quasi-simultaneous NIR to optical spectrum of the source.
2. Additionally, adding a thermal bremsstrahlung emission from a plasma of temperature 25 keV with log parabola also provides an acceptable statistical fit to the X-ray data, but is inconsistent with the optical spectrum as well as the general X-ray spectral properties of the source.
3. Accretion-disk-based models: reflection and cool Comptonization (Table 1) with an intrinsic power-law component describes 2015 optical to X-ray spectrum statistically well, and is consistent with the general spectral characteristics of OJ 287. Timing analysis indicates a lag of UV emission with respect to X-rays (Section 3.2), favoring reflection model. Additionally, these models also favor a heavy SMBH of mass  $\sim 10^{10} M_{\odot}$  for OJ 287, as has been argued by Sillanpää et al. (1988) and Lehto & Valtonen (1996) in interpreting the  $\sim 12$  yr optical QPO in a binary SMBH framework.

Furthermore, the appearance of the soft excess during 2015 and its absence in 2018 is consistent with the presence of accretion-disk signature (NIR–optical break) between 2013 May to 2016 November. Based on these considerations, the soft X-ray excess and UV emission appear to be primarily a result of *reflection phenomena*.

The authors gratefully acknowledge the anonymous referee for the thoughtful suggestions and comments which improved the manuscript. M.P. thanks the financial support of UGC, India program through DSKPDF fellowship (grant No. BSR/2017-2018/PH/0111). M.P. is also grateful for support of Prof. M. Sami at the Centre for Theoretical Physics, Jamia Millia Islamia, New Delhi. P.K. acknowledge funding from FAPESP (grant No. 2015/13933-0). This research has made use of archival data of *XMM-Newton* observatory, an ESA science mission directly funded by ESA Member States and NASA by the NASA Goddard Space Flight Center (GSFC). This research has also made use of the XRT Data Analysis Software (XRTDAS) developed under the responsibility of the ASI Science Data Center (ASDC), Italy.

*Facilities:* *Swift* (XRT and UVOT), *XMM Newton*.

*Software:* HEASOFT (<https://heasarc.gsfc.nasa.gov/docs/software/heasoft/>), GnuPlot (version: 5.0; <http://www.gnuplot.info/>).

## ORCID iDs

Main Pal  <https://orcid.org/0000-0001-6523-6522>

Pankaj Kushwaha  <https://orcid.org/0000-0001-6890-2236>

G. C. Dewangan  <https://orcid.org/0000-0003-1589-2075>

P. K. Pawar  <https://orcid.org/0000-0003-3188-1501>

## References

Abdo, A. A., Ackermann, M., Agudo, I., et al. 2010, *ApJ*, **716**, 30  
Alexander, T. 2013, arXiv:1302.1508

- Arnaud, K. A. 1996, in ASP Conf. Ser. 101, *Astronomical Data Analysis Software and Systems V*, ed. G. H. Jacoby & J. Barnes (San Francisco, CA: ASP), 17
- Britzen, S., Fendt, C., Witzel, G., et al. 2018, *MNRAS*, **478**, 3199
- Buisson, D. J. K., Lohfink, A. M., Alston, W. N., & Fabian, A. C. 2017, *MNRAS*, **464**, 3194
- Cackett, E. M., Fabian, A. C., Zoghbi, A., et al. 2013, *ApJL*, **764**, L9
- Crummy, J., Fabian, A. C., Gallo, L., & Ross, R. R. 2006, *MNRAS*, **365**, 1067
- D’Ammando, F., Larsson, J., Orienti, M., et al. 2014, *MNRAS*, **438**, 3521
- Dauser, T., Garcia, J., Wilms, J., et al. 2013, *MNRAS*, **430**, 1694
- Dauser, T., Wilms, J., Reynolds, C. S., & Brenneman, L. W. 2010, *MNRAS*, **409**, 1534
- Dickey, J. M., & Lockman, F. J. 1990, *ARA&A*, **28**, 215
- Done, C., Davis, S. W., Jin, C., Blaes, O., & Ward, M. 2012, *MNRAS*, **420**, 1848
- Edelson, R. A., & Krolik, J. H. 1988, *ApJ*, **333**, 646
- Fabian, A. C., Zoghbi, A., Ross, R. R., et al. 2009, *Natur*, **459**, 540
- Gabriel, C., Denby, M., Fyfe, D. J., et al. 2004, in ASP Conf. Ser. 314 *Astronomical Data Analysis Software and Systems (ADASS) XIII*, ed. F. Ochsenbein, M. G. Allen, & D. Egret (San Francisco, CA: ASP), 759
- García, J., Dauser, T., Lohfink, A., et al. 2014, *ApJ*, **782**, 76
- García, J., Dauser, T., Reynolds, C. S., et al. 2013, *ApJ*, **768**, 146
- García, J., Kallman, T. R., & Mushotzky, R. F. 2011, *ApJ*, **731**, 131
- Gaur, H., Mohan, P., Wiercholska, A., & Gu, M. 2018, *MNRAS*, **473**, 3638
- Ghosh, R., Dewangan, G. C., Mallick, L., & Raychaudhuri, B. 2018, *MNRAS*, **479**, 2464
- Gierliński, M., & Done, C. 2004, *MNRAS*, **349**, L7
- Goyal, A., Stawarz, L., Zola, S., et al. 2018, *ApJ*, **863**, 175
- Gupta, A. C., Agarwal, A., Mishra, A., et al. 2017, *MNRAS*, **465**, 4423
- Gupta, A. C., Kalita, N., Gaur, H., & Duorah, K. 2016, *MNRAS*, **462**, 1508
- Hudec, R., Bašta, M., Pihajoki, P., & Valtonen, M. 2013, *A&A*, **559**, A20
- Idesawa, E., Tashiro, M., Makishima, K., et al. 1997, *PASJ*, **49**, 631
- Isobe, N., Tashiro, M., Sugiho, M., & Makishima, K. 2001, *PASJ*, **53**, 79
- Kapanadze, B., Vercellone, S., Romano, P., et al. 2018, *MNRAS*, **480**, 407
- Kushwaha, P., de Gouveia Dal Pino, E. M., Gupta, A. C., & Wiita, P. J. 2019, arXiv:1901.10768
- Kushwaha, P., Gupta, A. C., Wiita, P. J., et al. 2018a, *MNRAS*, **473**, 1145
- Kushwaha, P., Gupta, A. C., Wiita, P. J., et al. 2018b, *MNRAS*, **479**, 1672
- Kushwaha, P., Sahayanathan, S., & Singh, K. P. 2013, *MNRAS*, **433**, 2380
- Lehto, H. J., & Valtonen, M. J. 1996, *ApJ*, **460**, 207
- Leighly, K. M. 1999, *ApJS*, **125**, 317
- McHardy, I. M., Cameron, D. T., Dwelly, T., et al. 2014, *MNRAS*, **444**, 1469
- McHardy, I. M., Connolly, S. D., Horne, K., et al. 2018, *MNRAS*, **480**, 2881
- Mehdipour, M., Branduardi-Raymont, G., Kaastra, J. S., et al. 2011, *A&A*, **534**, A39
- Miniutti, G., & Fabian, A. C. 2004, *MNRAS*, **349**, 1435
- Nilsson, K., Takalo, L. O., Lehto, H. J., & Sillanpää, A. 2010, *A&A*, **516**, A60
- Pal, M., Dewangan, G. C., Connolly, S. D., & Misra, R. 2017, *MNRAS*, **466**, 1777
- Pal, M., Dewangan, G. C., Kembhavi, A. K., Misra, R., & Naik, S. 2018, *MNRAS*, **473**, 3584
- Pal, M., Dewangan, G. C., Misra, R., & Pawar, P. K. 2016, *MNRAS*, **457**, 875
- Pal, M., & Naik, S. 2018, *MNRAS*, **474**, 5351
- Peterson, B. M., Wanders, I., Horne, K., et al. 1998, *PASP*, **110**, 660
- Qian, S. 2018, arXiv:1811.11514
- Seta, H., Isobe, N., Tashiro, M. S., et al. 2009, *PASJ*, **61**, 1011
- Shi, W., Liu, X., & Song, H. 2007, *Ap&SS*, **310**, 59
- Siejkowski, H., & Wiercholska, A. 2017, *MNRAS*, **468**, 426
- Sillanpää, A., Haarala, S., Valtonen, M. J., Sundelius, B., & Byrd, G. G. 1988, *ApJ*, **325**, 628
- Sillanpää, A., Takalo, L. O., Pursimo, T., et al. 1996a, *A&A*, **305**, L17
- Sillanpää, A., Takalo, L. O., Pursimo, T., et al. 1996b, *A&A*, **315**, L13
- Sitko, M. L., & Junkkarinen, V. T. 1985, *PASP*, **97**, 1158
- Stickel, M., Fried, J. W., & Kuehr, H. 1989, *A&AS*, **80**, 103
- Tanaka, Y., Nandra, K., Fabian, A. C., et al. 1995, *Natur*, **375**, 659
- Turner, M. J. L., Abbey, A., Arnaud, M., et al. 2001, *A&A*, **365**, L27
- Valtonen, M. J., Ciprini, S., & Lehto, H. J. 2012, *MNRAS*, **427**, 77
- Valtonen, M. J., Zola, S., Ciprini, S., et al. 2016, *ApJL*, **819**, L37
- Visvanathan, N., & Elliot, J. L. 1973, *ApJ*, **179**, 721
- Zdziarski, A. A., Johnson, W. N., & Magdziarz, P. 1996, *MNRAS*, **283**, 193
- Zu, Y., Kochanek, C. S., & Peterson, B. M. 2011, *ApJ*, **735**, 80
- Życki, P. T., Done, C., & Smith, D. A. 1999, *MNRAS*, **309**, 561